Rapidly Cooled Polyethylenes: On the Thermal Stability of the Semicrystalline Morphology

M. Basiura,[†] R. I. Gearba,[‡] D. A. Ivanov,[‡] J. Janicki,[§] H. Reynaers,[†] G. Groeninckx,[†] W. Bras,[⊥] and B. Goderis*,[†]

Chemistry Department, Molecular and Nanomaterials, Catholic University of Leuven, Celestijnenlaan 200F, B3001 Heverlee, Belgium; Laboratoire de Physique des Polymères, CP-223, Université Libre de Bruxelles, Bld. du Triomphe, B-1050, Brussels, Belgium; Institude of Textile Engineering and Polymer Materials, University of Bielsko-Biala, ul. Willowa 2, 43-300 Bielsko-Biala, Poland; and DUBBLE-CRG/ESRF, Netherlands Organization for Scientific Research (NWO), B.P. 220, F-38043 Grenoble Cedex, France

Received March 16, 2006; Revised Manuscript Received September 15, 2006

ABSTRACT: During rapid cooling at about 1000 °C/min linear polyethylene crystallizes into spherulitically organized, semicrystalline lamellar stacks. The crystals contain chain conformational defects that are expelled upon reheating. Concomitantly, the crystal grain size increases and surface melting is observed. Close to the melting offset some crystals melt and recrystallize. The crystalline density does not differ from the density of perfect orthorhombic material at any temperature. Small-angle X-ray scattering (SAXS) reveals that the amorphous fraction only completely devitrifies above ∼17 °C. A quench-cooled homogeneous copolymer of ethylene with 5.2 mol % 1-octene devitrifies at −50 °C during heating and displays highly branched crystals with a considerable amount of homogeneously distributed defects. Upon heating, these defects migrate toward the crystal surface while crystal fragments and branches preferentially melt, thus leading to an increase of the average crystal lateral dimensions. At rather high temperatures even the most stable crystals melt and recrystallize. The new methodology adopted to extract the crystal lateral dimensions from the SAXS patterns was also applied to the correlation functions calculated from binarized (high-temperature) AFM images. The results are comparable.

1. Introduction

The crystallization of linear polyethylene at high supercooling is very fast due to its simple regular chain microstructure. The maximum achievable spherulite growth rate is a matter of debate,[1] but rates of 70 μm/s at 90 °C[2] and 2 m/s at 80 °C[3] have been observed. As a result, even the quenching of 100 nm thick polyethylene films in dichlorodifluoromethane at its melting point (−155 °C) readily yields spherulitically arranged, crystalline lamellae rather than a glassy state.[4] The formation of glassy, amorphous material was only reported after quenching in a solid/liquid nitrogen mixture.[4] Samples with a 30 μm thickness, quenched in milder media, like e.g. liquid nitrogen,[5] do not reveal sharp X-ray[6] or electron diffraction reflections[4] as one would expect from semicrystalline material. Nevertheless, it is believed that this material is not truly amorphous but consists of small nodular, poorly ordered crystal (precursor) entities.[4] Sharp diffraction peaks only appear after heating to approximately −80 °C because at that temperature the chains have gained sufficient mobility. At room temperature the crystallinity tends to 60%.[6]

These real-time crystallization experiments are demanding since high cooling rates have to be realized and fast detection systems are needed. Quite successful is the approach by Ding and Spruiell, who performed quench experiments with depolarized light microscopy.[7−9] With such equipment crystallization at high, but nonconstant, cooling rates can be examined, with instantaneous quenching rates up to −5000 °C/min. Under such conditions the solidification of isotactic polypropylene (iPP) and high-density polyethylene (HDPE) is so fast and extensive that at a given temperature during the cooling run the heat released by crystallization cannot be dissipated by the cooling medium.[7,10,11] This results in an isothermal plateau in the time−temperature profile where consequently crystallization happens "pseudo-isothermally". An increase in the cooling rate lowers the plateau temperature. Most of the crystallinity develops at this stage in the case of HDPE and iPP. In contrast with these findings, the crystallinity level reached by low-density polyethylene (LDPE) under such pseudo-isothermal conditions is rather low, and higher crystallinity values are only obtained upon further cooling, which most likely involves chains with a lower molecular weight and/or a higher branching degree.[7]

Similar observations have been reported for homogeneous ethylene−α-olefin copolymers[12] polymerized by vanadium- or metallocene-based catalysts[13] and characterized by a uniform short chain branching (SCB) distribution within and in between chains. Most of the homogeneous copolymers display a broad crystallization temperature range. The crystallinity reached under pseudo-isothermal crystallization is negligible compared to what is observed for linear polyethylene (LPE), at least at moderate degrees of supercooling. The idea has been put forward that a temperature plateau is maintained as long as primary crystallization proceeds, i.e., the growth of spherulites.[2,14] Secondary crystallization, which is the slower crystallization of amorphous inclusions inside the spherulites, follows at lower temperatures. With lower comonomer content, more crystallinity is generated during primary crystallization.

At comparable shallow degrees of supercooling, spherulites of copolymers with a 1-octene content below 2.2 mol % grow slower than in LPE samples at the isothermal plateau.[2,14] This reduction in spherulite growth rate has been associated with

[†] Catholic University of Leuven.
[‡] Université Libre de Bruxelles.
[§] University of Bielsko-Biala.
[⊥] Netherlands Organization for Scientific Research (NWO).
* Corresponding author: e-mail bart.goderis@chem.kuleuven.be; Ph +32 16 327806, Fax +32 16 327990.

10.1021/ma060588f CCC: $33.50
Published on Web 10/26/2006

the creation of an intermediate disordered phase that only in a secondary stage converts into orthorhombic material.[2] A similar process was suggested to explain the high-temperature isothermal crystallization and double melting behavior of an ethylene−1-octene copolymer with 5.2 mol % 1-octene.[15] The latter work partially builds further on the findings by Strobl et al.[16]

However, the difference in spherulite growth rate between LPE and the copolymers (with a 1-octene contents at or below 2.2 mol %) decreases with increasing supercooling and disappears at a supercooling of about 50 °C.[2] Here it was suggested that the intermediate phase is absent and that the growth rate is controlled by the formation rate of small, partially ordered clusters on the crystal growth face whose disorder level depends on the supercooling.[2] Based on FTIR experiments, a similar crystallization mechanism involving the formation of trans segments in the melt followed by clustering into small crystallites and finally a growth into lamellae was suggested by Tashiro et al.[17]

The crystallization schemes discussed above are multistep processes toward—in principle—the morphology with the lowest free energy. Most likely, this most stable morphology in the case of homogeneous ethylene copolymers resembles the one described by Flory in his equilibrium copolymer crystallization theory.[18] In this theory it is postulated that the comonomer units are expelled from the crystals and that only ethylene sequences exceeding a critical length can crystallize at a given temperature. The crystallinity and lamellar crystal thickness distribution are thus completely determined by the ethylene sequence length distribution (ESLD). In homogeneous ethylene−1-octene copolymers, the ESLD is unimodal and the ethylene sequences are separated by hexyl branches. It has been observed that after crystallization at moderate supercooling the latter are indeed expelled from the orthorhombic polyethylene crystals.[19−22] However, as the free energy difference between the supercooled melt and that associated with the most stable (Flory) morphology increases with increasing supercooling, more "space" and "freedom" are given to intermediate, metastable structures and perhaps new, disordered or mesomorphic phases.

The conversion of these metastable morphologies, generated during fast cooling, into more stable ones requires mobility and accordingly temperatures above the glass transition temperature, T_g. However, even above T_g this does not readily occur! At high supercooling, polymer chains are frozen in by local solidification while retaining their melt chain conformation.[14] Accordingly, any given chain is likely to be part of several small crystallites. For a conversion toward stability, all these crystallites should be involved in a cooperative way in order to allow for a reasonable conformational chain change, which is very unlikely. Therefore, heating and cooperative melting and recrystallization seems to be the only way to achieve higher stability, as was suggested earlier to explain the melting behavior of a quenched homogeneous ethylene copolymer with 5.2 mol % 1-octene.[23] In the work described here the same material[23−26] is investigated more thoroughly. The structural changes during stepwise heating from room temperature are monitored in real space by using temperature-dependent atomic force microscopy (AFM). This approach reveals substantial deviations from the classical lamellar model, and accordingly new routes are developed to interpret the associated synchrotron small-angle X-ray scattering (SAXS) patterns. The AFM images are processed to yield correlation and interface distribution functions (IDF) similar to the ones that can be obtained from SAXS.

In order not to miss the actual low-temperature structure induced by rapid cooling and the structural changes involved between the glass transition temperature and room temperature, a special on-line quenching device was developed for the X-ray scattering experiments. Average cooling rates of around −1000 °C/min could be achieved even to temperatures below T_g. Accordingly, the structural changes during the heating at 10 °C/min, after the quenching, could be characterized between this temperature and the high-temperature melt state. Further characterizations were performed using small-angle light scattering (SALS). A LPE sample is treated and analyzed in a similar way for comparison. This sample has also been the subject of earlier publications.[27,28]

2. Experimental Section

2.1. Materials. The linear polyethylene (DSM code: JW1114) used has a M_w of 52 300 g/mol and a polydispersity of 2.8 and was prepared with a vanadium-based catalyst just like the homogeneous ethylene−1-octene copolymer (DSM code: JW1120) that contains 5.2 mol % 1-octene and has a molar mass (M_w) of 30 800 g/mol and a polydispersity of 2.

2.2. Temperature Program. For the AFM study, thin samples were melt compression molded between two glass platelets. After cooling, one of the plates was removed while the assembly was immersed in liquid nitrogen, thus leaving one free surface. Next, the samples were reheated to 200 °C and quenched after 5 min into acetone at freezing point (−95 °C) with the polymer melt directly in contact with the cold nonsolvent. All temperature treatments were conducted in a nitrogen atmosphere. The free surface of the copolymer sample was examined by AFM at stepwise increasing temperatures without any further treatment. Heating between the steps was conducted at 10 °C/min. At a given temperature 10 min was allowed for sample equilibration whereafter data were collected during typically 20 min, allowing considerable sample annealing. The LPE sample was only examined at room temperature. Copolymer topography and phase images were taken at room temperature, 80 °C, and 97 °C. The last temperature is in the middle of the DSC main melting peak.

For time-resolved synchrotron X-ray experiments, copolymer and LPE samples were quenched from the melt at 150 °C to −56 °C. Details of the cooling profile are discussed in section 2.3. After 2 min at −56 °C the samples were heated to 150 °C at 10 °C/min while collecting simultaneous SAXS and wide-angle X-ray diffraction (WAXD) patterns in consecutive time frames of 6 s.

Samples (50 μm thick) for SALS were melt compression molded between two glass coverslips and quenched into acetone at its freezing point (−95 °C) prior to heating at 10 °C/min starting from 40 °C.

2.3. SAXS−WAXD Quenching Device. To achieve fast cooling, a commercial Mettler FP-82 HT hot stage, flushed with cold nitrogen, was extended with a homemade, resistively heated oven equipped with a TCU01004 (Red Lion) temperature controller. The 0.5 mm thick samples were sealed in small brass rings with 15 μm thick aluminum foils where the X-ray beam passes.[28] These rings were fixed to a metallic frame that can be injected from the external oven into the FP-82 HT hot stage via the side entrance. Special brass plates were stuck to the FP-82 HT lid and the bottom furnaces to improve the heat transfer when the thin hot samples (150 °C) are shot into the cold FP-82 HT (−56 °C). The temperature in the hot stage during the quench and subsequent heating was controlled by a Mettler FP-90HT controller.

The WAXD patterns of a LPE sample, collected in time frames of 1 s during the quench, were evaluated to obtain an estimate of the quenching-induced temperature profile *inside* the polyethylene samples. In this case crystallization was complete within 2 s, as illustrated in Figure 1.

This figure shows the evolution of the LPE orthorhombic reflections during the first 8 s after triggering the quench. The positions of these reflections shift to higher angles during cooling as is expected for a contracting crystalline unit cell. The 200 reflection, in particular, is temperature sensitive and was used as a

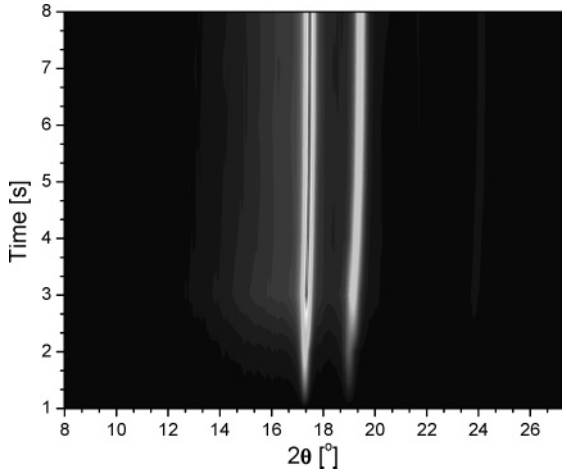

Figure 1. Evolution of the 110 and 200 orthorhombic reflections during the first 8 s after shooting molten LPE, with an initial temperature of 150 °C, into the Mettler hot stage which was set at −56 °C.

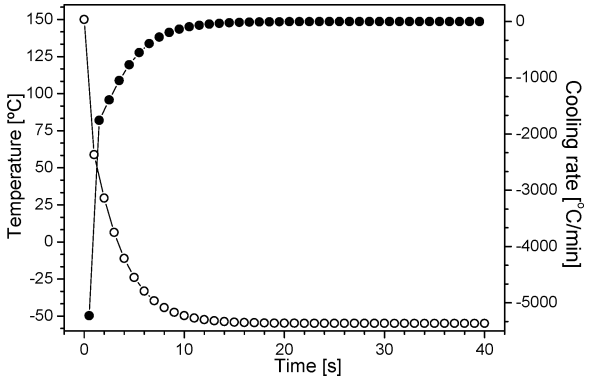

Figure 2. Cooling rate (full circles, right-hand scale) and estimated temperature (open circles, left scale) of the LPE sample during quenching as derived from the WAXD peak position evolution.

temperature probe. The relation between the 200 angular position and temperature was derived from time-resolved WAXD patterns, collected in a heating run at 10 °C/min. In Figure 2 the quench temperature profile and the cooling rate as a function of time are depicted.

2.4. SALS. SALS data were collected on a homemade apparatus.[15] Alternatingly, *Hν* (polarizer and analyzer perpendicular) and *Vν* (polarizer and analyzer parallel) configurations were obtained by flipping the analyzer every 3 s. Two-dimensional scattering patterns were digitally recorded every 3 s for 200 ms on a Photometrix ATC200L CCD camera, which results in an actual *Hν* or *Vν* SALS time resolution of one pattern every 6 s (or every °C), but staggered by 3 s (or 0.5 °C). For temperature control a Mettler FP-82HT hot stage was used. The relative total light scattering intensity of each pattern was obtained by integrating over both scattering and azimuthal angle (referred to as $Q_{Hν}$ and $Q_{Vν}$ for an *Hν* or *Vν* configuration, respectively), which for spherulitically arranged crystal aggregates can be written as[29,30]

$$Q_{Hν} = \frac{K}{15}\langle\delta^2\rangle = \frac{K}{15}\phi_{sp}(\phi_{csp}\delta^0_{cr}P_2)^2 \tag{1}$$

$$Q_{Vν} = K\left[\phi_{sp}(1-\phi_{sp})(\overline{\alpha_{sp}}-\alpha_0)(\alpha_t-\alpha_0) + \langle\delta^2\rangle\left(\frac{1}{5}-\frac{\phi_{sp}}{9}\right)\right] \tag{2}$$

where K is a constant,[30] ϕ_{sp} is the volume fraction of spherulites, ϕ_{csp} is the volume fraction crystallinity in a spherulite, δ^0_{cr} is the intrinsic anisotropy of a pure crystal, P_2 is a Hermans-type orientation function describing the orientation of the crystals with respect to the spherulite radius, $\overline{\alpha_{sp}}$ is the average optical polarizability of the spherulite, α_0 is the polarizability of the matrix surrounding the spherulite, and α_t is the tangential polarizability of the spherulite.

2.5. AFM. Atomic force microscopy (AFM) imaging, at variable temperature, was performed in tapping mode using a MultiMode, Nanoscope IIIA, Digital Instruments/Veeco Metrology Group, equipped with a modified high-temperature heating stage.[31] The latter includes a plug-in sample heater and a resistive heater for the probe, which is integrated into the probe holder. To image the polymer surface in thermal equilibrium, the temperatures of the sample and the probe were adjusted as described elsewhere.[32] To avoid sample surface damage by the scanning AFM tip at elevated temperatures, soft Si cantilevers (Mikromasch, Estonia) and light tapping conditions were adopted.

2.6. AFM Data Processing. The quantitative analysis of the AFM images was performed in reciprocal space, i.e., similar to the treatment of SAXS curves.[32−34] In the first step the images (phase image for room temperature and topography image for the higher temperatures) were converted into a binary (i.e., two-phase) image of which the (hard or high) parts (represented in white) are crystalline and the (soft or low) parts (represented in black) are liquidlike amorphous, using object recognition routines written in Igor Pro (Wavemetrics Ltd.). Such an image allows the surface crystallinity to be calculated by determining the fraction of white in the image, i.e., white/(white + black).

Next, two-dimensional power spectral density functions ($P_2(\mathbf{q})$) were computed from the binary AFM images ($u(\mathbf{r})$) up to the critical, or Nyquist, frequency. This frequency is dependent upon the experimental sampling interval:

$$P_2(\mathbf{q}) \equiv \frac{1}{A}\left|\int_A u(\mathbf{r})\, W(\mathbf{r}) \exp(i\mathbf{qr})\, \mathrm{d}^2\mathbf{r}\right|^2 \tag{3}$$

where A denotes the image area, $W(\mathbf{r})$ the window function,[35] and $\mathbf{q}$ the 2D reciprocal space vector. The $P_2(\mathbf{q})$ function was then transformed into a one-dimensional power spectral density ($P_1(q)$), where q stands for the norm of $\mathbf{q}$, according to

$$P_1(q) = \frac{\int P_2(\mathbf{q}')\delta(|\mathbf{q}'| - q)\, \mathrm{d}\mathbf{q}'}{q} \tag{4}$$

Finally, the one-dimensional correlation function,[36] which is directly comparable with the correlation function that can be derived from SAXS experiments, was computed as the real part of the Fourier transform of $P_1(q)$:

$$\gamma(x) \cong \mathrm{Re}\{2\pi\int_0^\infty P_1(q) q \exp(iqx) \exp(q^2\sigma^2)\, \mathrm{d}q\} \tag{5}$$

where x is the coordinate in real space and the exponential factor σ—in principle—serves to correct for the presence of a sigmoidal gradient crystal/amorphous transition layers with a thickness 3σ.[37] Obviously, in binary images such gradients cannot be present, but it seems that the microroughness on the edges between black and white domains in the micrographs gives rise to a similar negative deviation from Porod's law as can be found in X-ray scattering curves of materials where such a density gradient is present.

This microroughness is potentially a sample characteristic, but it can also be influenced by the image quality and binarization procedure. The function $\gamma(x)$ was normalized to 1 at the origin ($x = 0$) and further processed similarly to the SAXS-based correlation functions as explained in the SAXS processing section below. The interface distribution function (or chord length distribution function) $\gamma''(x)$ defined here as the convolution of the first derivative of the density profile across the lamellar stack

$$\gamma''(x) = \frac{\mathrm{d}\rho(x)}{\mathrm{d}x} \otimes \frac{\mathrm{d}\rho(-x)}{\mathrm{d}x} \tag{6}$$

was calculated as the second derivative of $\gamma(x)$:

$$\gamma''(x) = \frac{d^2\gamma(x)}{dx^2} \tag{7}$$

Finally, $\gamma''(x)$ was used to calculate the most probable crystal chord length (l_c) since $\gamma''(x)$ can be expanded in a series of different chord length distribution functions with alternating signs:[38]

$$\gamma''(x) \cong h_c(x) + h_a(x) - 2h_{ac}(x) + ... \tag{8}$$

The first three distribution terms in (8) are of particular interest for the present study, i.e., the crystal chord length distribution, $h_c(x)$, the interlamellar amorphous region, $h_a(x)$, and the intercrystalline distance, $h_{ac}(x)$. The last term is often referred to as the long period.

2.7. Synchrotron SAXS and WAXD. Time-resolved, simultaneous SAXS/WAXD experiments were carried out at the Dutch-Belgian Beamline (DUBBLE-CRG, ESRF, Grenoble, France).[39] SAXS data were recorded on a quadrant[40] detector and WAXD data on a curved, microstrip detector[41] using an X-ray wavelength of 1.24 Å. The WAXD and SAXS patterns were corrected for the detector response and normalized to the intensity of the transmitted beam measured by an ionization chamber placed downstream from the sample. The latter procedure corrects for primary beam intensity decay and accounts for changes in sample transmission. The scattering vector axis, q (with $q = (4\pi/\lambda)(\sin\theta)$, 2θ the scattering angle and λ the wavelength), of the SAXS region was calibrated using the first nine orders of dry collagen. The 110 and 200 reflections of the LPE sample at room temperature were used to calibrate the WAXD 2θ axis.

2.8. WAXD Data Processing. A linear background was subtracted from the WAXD data, which were collected over the angular range $7° \le 2\theta \le 67°$. The experimental curves were fitted with a linear combination of a Lorentz function (describing the amorphous halo) and Pearson functions for the 110 and the 200 reflections, using the Marquardt−Levenberg nonlinear least-squares curve-fitting algorithm as implemented in Microcal Origin (version 6.0, Microcal Software, Inc., Northampton, MA). Figure 3 illustrates the outcome of such a procedure for the quenched LPE sample at −56 °C, together with a set of copolymer WAXD patterns at temperatures equal to the SAXS data selection in Figure 5 (see below).

The mass fraction of orthorhombic crystalline material was calculated as the ratio of the area under the 110 and 200 crystalline peaks to the total area under the scattering curve. An estimate of the crystallite size, D_{110}, in a direction perpendicular to the reflecting 110 planes was obtained by applying the Scherrer equation:[42]

$$D_{hkl} = \frac{\lambda}{\beta_0 \cos\theta} \tag{9}$$

β_0 is the full width at half-maximum of the 110 reflection. This is an estimated minimum since peak broadening due to instrumental factors, paracrystalline distortions, and microstrain are not separately treated. The crystalline density was calculated from the angular positions of the 110 and 200 Pearson's maxima under the assumption that the length of the orthorhombic unit cell in the c axis direction (the molecular chain direction) is constant and equal to 2.547 Å.

Finally, the WAXD crystallinities were converted into volume fractions using the temperature-dependent orthorhombic crystalline density [g cm^{-3}], ρ_c

$$\rho_c = \frac{1}{0.994 + 2.614 \times 10^{-4} T + 4.43 \times 10^{-7} T^2} \tag{10}$$

of LPE reported by Swan[43] and the temperature-dependent amorphous density [g cm^{-3}], ρ_a, relevant to semicrystalline polyethylene

$$\rho_a = 8.5769 \times 10^{-1} - 6.1820 \times 10^{-4} T + 4.6409 \times 10^{-7} T^2 \tag{11}$$

obtained by independent absolute SAXS measurements.[44] In both eq 10 and eq 11 the temperature, T, is expressed in °C. In this conversion the deviation when the experimental WAXD-based crystalline densities would be used instead of the Swan values would be negligibly small.

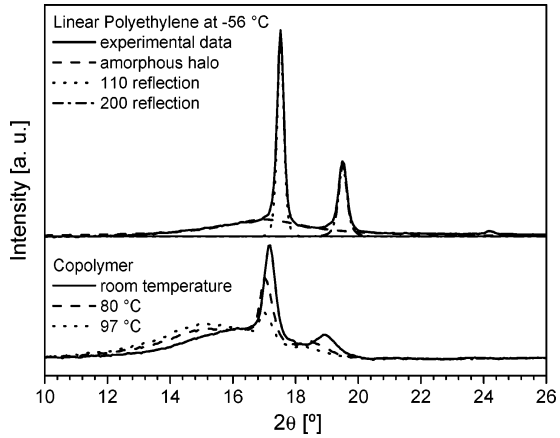

Figure 3. Decomposed WAXD pattern of LPE at −56 °C (top) and copolymer WAXD patterns at selected temperatures (bottom).

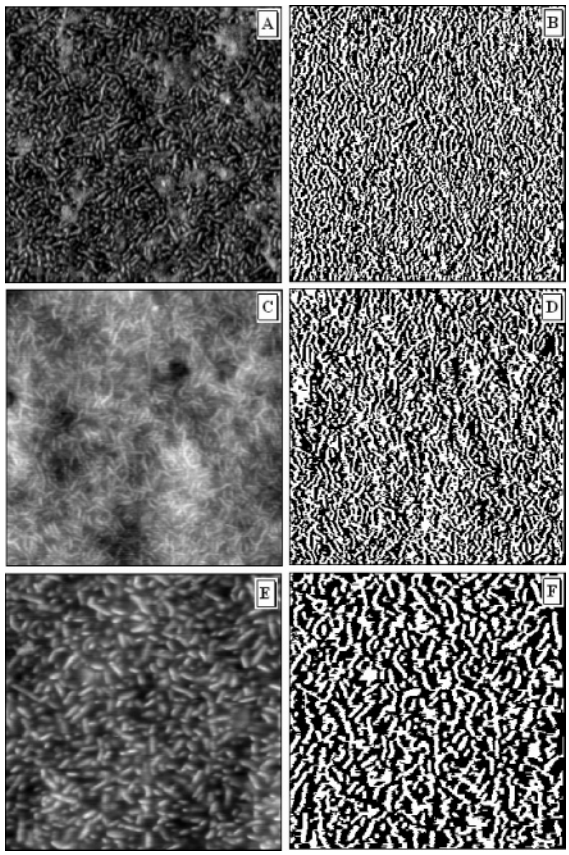

Figure 4. Phase image of the quenched copolymer at room temperature (A) with corresponding binary image (B), topography image of the quenched copolymer after heating to 80 °C (C) with corresponding binary image (D), and topography image of the quenched copolymer after heating to 97 °C (E) with the corresponding binary image (F). All images are 1 μm by 1 μm.

2.9. SAXS Data Processing. An averaged melt pattern was subtracted as a background from the SAXS patterns, which were collected over the scattering vector range $0.0094 \le q \le 0.2136$ Å^{-1}. The resulting raw data, $I_{raw}(q)$, were fitted in the range $0.0691 \le q \le 0.2136$ Å^{-1} with eq 12,[37] substituted by the fitting results and extrapolated to $q = 0.56$ Å^{-1} after subtracting the background B as described earlier:[27]

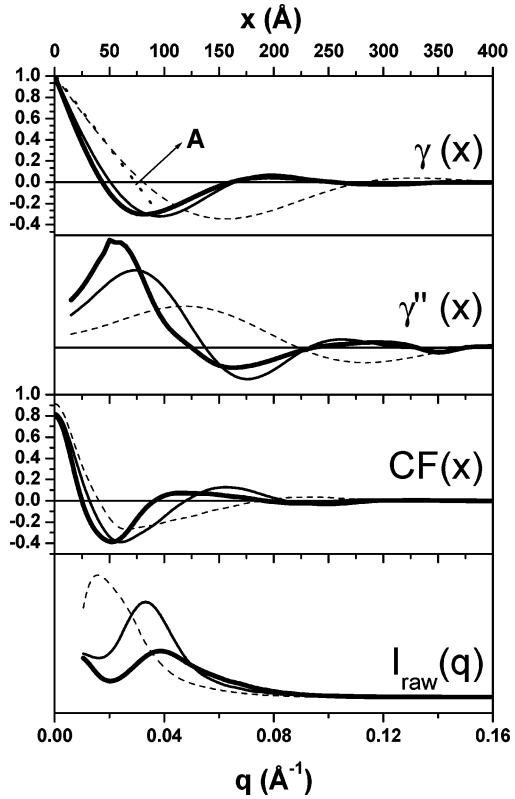

Figure 5. AFM-based $\gamma(x)$ and $\gamma''(x)$ functions for the quenched copolymer at room temperature (thick full lines), 80 °C (thin full lines), and 97 °C (dashed lines) together with the corresponding SAXS based CF(x) functions and raw data, $I_{raw}(q)$, at the same temperatures. The dotted line added to the $\gamma(x)$ function at 97 °C is a linear regression to this function's autocorrelation triangle and illustrates how the parameter "*A*" is obtained.

$$B + \frac{P}{(q/2\pi)^4}\exp(-\sigma^2 q^2) \tag{12}$$

with P the Porod constant and σ a measure for the transition layer (cf. eq 5). After an appropriate extrapolation to zero angle,[27] $I(q)$ was obtained and linear correlation functions, $K(x)$, were calculated by a cosine transformation:

$$K(x) = \frac{1}{(2\pi)^3}\int_0^\infty (I(q)4\pi q^2 \cos qx)\, \mathrm{d}q \tag{13}$$

The fitting and extrapolation procedure using eq 12 merely helps avoiding truncation errors in the Fourier transformation but cannot be used to obtain reliable estimates for σ since fitting was performed in a limited angular range.[27] Therefore, further data interpretation occurred in terms of the corresponding ideal two-phase system, involving sharp crystalline−amorphous interfaces in the middle of the (artificial) interphase.[27] The (relative) invariant or total scattering power of the corresponding ideal two-phase structure, Q_{id}, is obtained from the intercept of the linear regression to the autocorrelation triangle[45]

$$Q_{id} = C\alpha_S\phi(1-\phi)(\rho_c - \rho_a)^2 \tag{14}$$

with C a temperature-independent constant, ϕ the local volume fraction of the minority phase in the semicrystalline regions, α_S the volume fraction of semicrystalline regions, and ρ_c and ρ_a the mass densities of the crystalline and amorphous phases, respectively. In principle, electron densities should be used in eq 14, but since only polyethylene is present, it is correct to put mass densities provided that a scaling factor is included in the constant C. After dividing $K(x)$ by Q_{id}, normalized correlation function are obtained, referred to as $CF(x)$.

At first all $CF(x)$ and AFM-based $\gamma(x)$ functions were processed in terms of a morphology that consists of stacks with alternating crystalline and amorphous layers that are (nominally) infinitely extended laterally. In this context ϕ is calculated from the correlation functions with the quadratic expression:[27]

$$A = \phi(1-\phi)L_P \tag{15}$$

where A represents the intersection of the linear regression to the autocorrelation triangle with the abscissa, L_P, the long period, obtained from the position of the first side-maximum in $CF(x)$ or $\gamma(x)$. Independent information is needed to decide whether ϕ corresponds to ϕ_L, the local crystallinity, or $(1-\phi_L)$, the local noncrystalline fraction. For the SAXS data the crystallinity values obtained from WAXD are used as a guideline, and ϕ was taken to be equal to ϕ_L for the copolymer over the full temperature range and to $(1-\phi_L)$ in the LPE case below 120 °C. At higher temperatures ϕ was put equal to ϕ_L. The AFM surface crystallinities are all below 0.5, and accordingly ϕ_L was associated with ϕ throughout. To obtain the lamellar thickness, l_c, ϕ_L was simply multiplied with L_P.

3. Results

The AFM images associated with the room temperature LPE sample reveal laterally extended lamellar stacks. This is in contrast to the copolymer sample, of which the 1 μm temperature-dependent images and corresponding binary versions are displayed in Figure 4.

At room temperature, the (bright) crystals are highly branched and the short alternating crystalline−amorphous layer stacks have finite lateral dimensions. At 80 °C the crystal thickness remains nearly unchanged compared to the room temperature situation, but the crystal lateral dimensions seem to have increased slightly. This is in contrast to the 97 °C morphology where much thicker crystals are observed, again with finite lateral dimensions. In Figure 5, the associated $\gamma(x)$ and $\gamma''(x)$ functions are displayed together with the corresponding SAXS-based $CF(x)$ functions obtained at the same temperatures.

In Table 1 the parameters obtained from the analysis of $\gamma(x)$ and $\gamma''(x)$ are summarized. The quantities labeled qe indicate that they were obtained using the quadratic equation (15). In $\gamma''(x)$ only one maximum is observed for $x < L_P$, and this was assigned to the crystal thickness distribution since this distribution was assumed to be sharper than the one of the amorphous regions. A crystallinity estimate, ϕ_L, was obtained from $\gamma''(x)$ by calculating l_c/L_P, with l_c and L_P obtained from the positive and negative local maxima in $\gamma''(x)$, respectively.

The crystallinity parameter ϕ_L obtained from $\gamma(x)$ is always lower than the true (model independent) crystallinity, which is the surface crystallinity, Φ. The $\gamma''(x)$-based ϕ_L estimates are closer to, but nevertheless also different from, the surface crystallinity. The former deviation, related to $\gamma(x)$, is due to the finite lateral dimensions of the crystals and the latter, related to $\gamma''(x)$, to the fact that the chords at the maxima of the distributions are "most probable", rather than "number-average" values.

However, using the true (surface) crystallinity, Φ, as input parameter, one can obtain the true number-average chord lengths and an estimate of the lateral dimensions of the lamellar crystals from the $\gamma(x)$ autocorrelation triangle. Equation 15 is in fact only relevant for stacks of lamellae with infinite lateral dimensions. The more general form of this equation reads

$$A = \phi(1-\phi)\frac{2}{O_S} \tag{16}$$

with O_S the local surface-to-volume ratio or specific surface.

Table 1. Morphological Parameters Derived from the Analysis of AFM Images at 25, 80, and 97 °C and from the Synchrotron SAXS and WAXD Patterns[a]

temperature	25 °C	80 °C	97 °C
	AFM		
surface crystallinity, Φ	0.47	0.47	0.42
ϕ_L from $\gamma(x)$ and qe	0.28	0.36	0.35
l_c from $\gamma(x)$ and qe (Å)	55	72	115
L_P from side max $\gamma(x)$ (Å)	190	200	330
l_c from pos max $\gamma''(x)$ (Å)	55	75	120
L_P from neg max $\gamma''(x)$ (Å)	165	175	285
ϕ_L from l_c/L_P of $\gamma''(x)$	0.30	0.43	0.42
$\langle l_c \rangle$ (Å)	75	87	129
$\langle l_a \rangle$ (Å)	84	98	178
$\langle l_c \rangle + \langle l_a \rangle$ (Å)	159	185	308
Y (Å)	407	1132	1929
l_c from ΦL_P (Å)	92	94	139
	SAXS		
ϕ_L from CF(x) and qe	0.28	0.28	0.21[b]
l_c from CF(x) and qe (Å)	34	44	50
L_P from side max CF(x) (Å)	123	155	234
WAXD crystallinity, Φ	0.42[b]	0.29[b]	0.12
$\langle l_c \rangle$ (Å)	43	44	50
$\langle l_a \rangle$ (Å)	58	110	184
$\langle l_c \rangle + \langle l_a \rangle$ (Å)	101	154	234
D (Å)	498	3748	infinite
α_S	1	1	0.56
l_c from $\phi_L L_P$ (Å)	52	45	50

[a] Most of the errors in the analysis of SAXS patterns, involving a correlation function approach, are systematic (related to the model) rather than statistic (related to the noise in the original data). Therefore, standard deviations are very small and not mentioned. The same holds for the AFM-based data. Here the selected binarization procedure adds to the systematic error. [b] Correct measure for ϕ_L.

For samples that are homogeneously filled by similar structures, O_S equals the overall specific surface, which is the case here. The position of A is illustrated in the 97 °C $\gamma(x)$ function in Figure 5. Furthermore

$$\langle l_c \rangle = \phi_L \frac{2}{O_S} = \frac{A}{1-\phi_L} \tag{17}$$

$$\langle l_a \rangle = (1-\phi_L)\frac{2}{O_S} = \frac{A}{\phi_L} \tag{18}$$

with $\langle l_c \rangle$ and $\langle l_a \rangle$ the number-average crystalline and amorphous chord lengths. Using Φ as input in eqs 17 and 18, the parameters $\langle l_c \rangle$ and $\langle l_a \rangle$ as well as their sum were calculated (see Table 1). Only for laterally infinitely extended lamellar systems this sum equals the number-average long period, $\langle L_P \rangle$.

Obviously, O_S depends on the crystal dimensions. We define platelike (lamellar) crystals with an average thickness parallel to the lamellar normal, l_c, and finite lateral dimensions Y and Z that are much larger than l_c. Generally, l_c differs from $\langle l_c \rangle$. Furthermore, the platelike crystals are stacked in a direction parallel to l_c and are separated by amorphous layers, with a thickness l_a in a direction parallel to the stacks. In the case of space-filling stacks and a number-average repeat distance between the crystalline plates, L_P (with $L_p = l_c + l_a$, which generally differs from $\langle l_c \rangle + \langle l_a \rangle$), one can write

$$O_S = \frac{2YZ + 2Y\phi L_p + 2Z\phi L_p}{YZL_p} \tag{19}$$

This equation contains the minority fraction, ϕ, which is equal to l_c/L_p (or ϕ_L) if $\phi_L < 0.5$ or to l_a/L_p (or $(1-\phi_L)$) if $\phi_L > 0.5$.

The $\gamma(x)$ functions, derived from 2D binary images, correspond to $\gamma(x)$ functions of 3D structures in which there are no structural changes in the direction normal to the observation plane. Obviously, these $\gamma(x)$ functions only yield realistic information about the crystal stacks when they are measured strictly edge-on, which is hard to meet. In a first approach we assume that all lamellar crystals were measured edge-on by AFM and that the third dimension of the crystals, Z, is perpendicular to the observation plane.

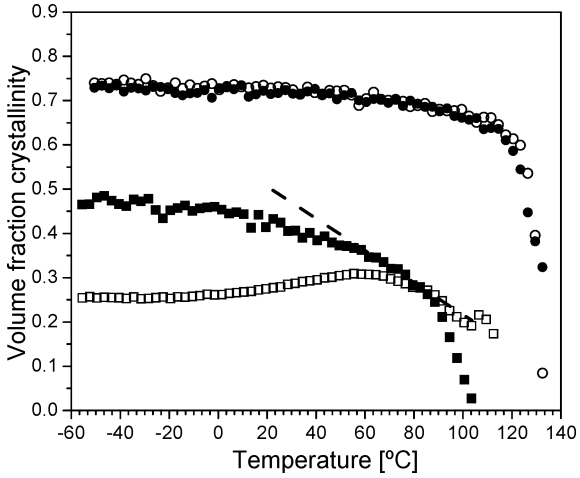

Figure 6. WAXD-based volume fraction crystallinity (full squares: copolymer; full circles: LPE) and SAXS-based ϕ_L values derived from the quadratic expression (open squares: copolymer; open circles: LPE) during heating at 10 °C/min. Only one point out of three is shown for clarity. The dashed line highlights the increased melting rate above 60 °C.

Using eq 19, we can extract the lamellar lateral dimensions under the assumption that the first side maximum in $\gamma(x)$ corresponds to L_P and that l_c can be calculated from $\phi_L L_P$, with $\phi_L = \Phi$. This implies that we assume that the "linear crystallinity" in a given stack is identical to the overall crystallinity, Φ. In this case we can rewrite eq 19 with the limiting condition imposed by the image that $Z \rightarrow \infty$:

$$O_S = \frac{2Y + 2\phi L_P}{YL_P} \tag{20}$$

Y is the lateral crystal dimension of interest in the 2D images and can be calculated from a combination of eqs 16 and 20, yielding

$$Y = \frac{AL_p\phi}{L_p\phi(1-\phi) - A} \tag{21}$$

The resulting Y values for the present images are included in Table 1 and are reasonable when compared to the structural features in the AFM images. Note that in the limiting case $Y \rightarrow \infty$ (i.e., for lamellar crystals with infinite lateral dimensions) in eq 21, one obtains eq 15 again, as is required.

The SAXS ϕ_L values obtained in terms of the lamellar model (eq 15) are represented in Figure 6 together with the WAXD-based overall degree of crystallinity after conversion to volume fraction.

The SAXS and WAXD crystallinities of the LPE sample agree well, except above 110 °C where the SAXS estimates are higher. Higher SAXS values at high temperatures (above 90 °C) are more clearly observed for the copolymer. These deviations are due to the formation of large, fully amorphous regions.[27] Here the fraction of semicrystalline regions, α_S, drops below 1:[27] the SAXS crystallinity equals ϕ_L and that of WAXD $\phi_L\alpha_S$. The deviation between the copolymer local SAXS and

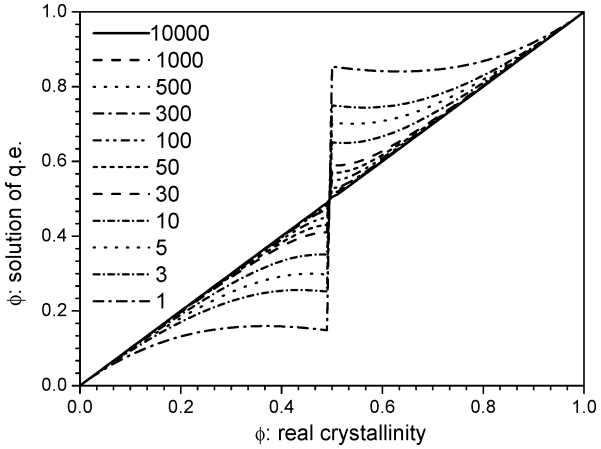

Figure 7. Effect of the lateral crystal size, expressed as m times L_P, with $L_P = 1$ on the crystallinity calculated from the quadratic equation. The factor *m* is varied according to the legend.

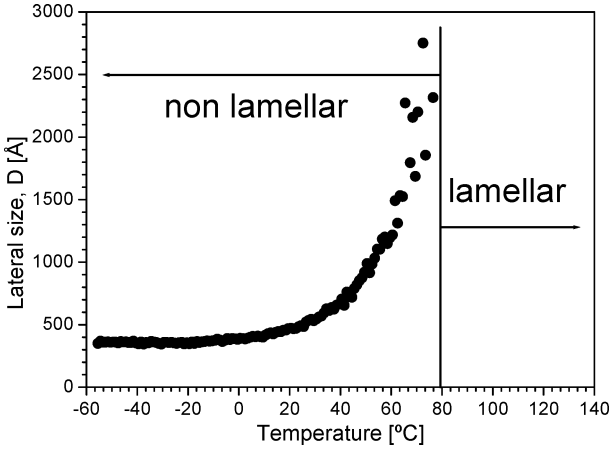

Figure 8. SAXS-based copolymer crystal lateral size evolution during heating. Above 80 °C the crystals have nominally infinite lateral dimensions and correspond to classical lamellae. The morphologies involving crystals with limited lateral dimensions are accordingly termed nonlamellar. Moreover, since the crystals are frequently branched, such morphologies resemble cocontinuous structures rather than semicrystalline stacks.

overall WAXD crystallinities in Figure 6 at low temperature, however, requires a different explanation since the AFM images all clearly reveal homogeneous and space-filling morphologies. For comparison with the AFM-based data, the SAXS ϕ_L values at the corresponding temperatures and based on eq 15 are added to Table 1 together with the associated l_c and L_P values (first three SAXS rows in the table).

Just like for the parameters obtained from AFM data, the discrepancy between the quadratic equation based ϕ_L values and the true, overall WAXD crystallinity, Φ, can be accounted for by considering the lateral size of the crystals. In SAXS, obviously, real 3D structures, rather than 2D images, are being probed. Therefore, there is no need to set any of the lateral sizes equal to infinity. However, to characterize the crystal lateral size, it is necessary to assume that the *Y* and *Z* lateral sizes are identical in order to get rid of one unknown and to obtain a solvable equation. Moreover, at this point there are no indications that reality is different. Replacing *Y* and *Z* by the common lateral dimension *D* in eq 19 and inserting the result in eq 16 yields a solution for *D*:

$$D = \frac{2AL_P\phi}{L_P\phi(1-\phi) - A} \tag{22}$$

It can easily be shown how the presence of finite lateral crystal dimensions result in too low ϕ_L values when eq 15 is used with undue care.

Using $L_p = 1$ as input and $D = mL_p$, *A* values were calculated using eq 22. ϕ_L was varied from 0 to 1. Accordingly, the minority fraction, ϕ, needed in eq 22, runs from 0 to 0.5 and beyond 0.5 again to 0. The parameter *m* was varied between 1 and 10 000. These *A* values were then inserted in eq 15 (again with $L_P = 1$), and solutions for ϕ were retrieved. The outcome of this exercise is illustrated in Figure 7 where the solution for ϕ is plotted as a function of the (true) input ϕ_L (for $\phi_L > 0.5$, $(1 - \phi)$ is plotted).

The deviation between the true crystallinity and the solution of the quadratic equation increases with smaller *m* (accordingly, smaller *D*) and also for true crystallinity values closer to 0.5. This is in agreement with earlier work.[23] Accordingly, the large low temperature deviation between SAXS and WAXD in Figure 6 can qualitatively be accounted for by assuming the existence of lamellae with finite lateral dimensions. In contrast, it is reasonable to conclude that the LPE lamellae are laterally extended since there are *no* such deviations. Moreover, similar ϕ_L values are obtained from the (flat) minimum in $CF(x)$,[27,45] confirming once more that the infinite lamellar model (eq 15) holds true for LPE.

Both L_P and *A* can be obtained directly from $CF(x)$. However, to calculate *D*, one also needs ϕ. For this parameter the WAXD crystallinity of the copolymer was taken below the overlap region between the WAXD- and SAXS-based estimates in Figure 6, i.e., around 80 °C. At and above that region the SAXS-based ϕ_L values were used (see Figure 8).

There is little or no evolution in *D* below 0 °C, but between 0 and 80 °C *D* increases rapidly toward (nominally) infinity. When *D* equals infinity (for SAXS), the infinite lamellar model holds true. In fact, beyond 80 °C, this was explicitly assumed since here the SAXS ϕ_L values from eq 15 were used, which resulted in a zero denominator in eq 22.

Using eqs 17 and 18 and taking the Φ and ϕ_L values as for the calculation of *D*, $\langle l_c \rangle$ and $\langle l_a \rangle$ were also calculated for the appropriate temperatures (see Table 1). The $\langle l_c \rangle$ parameters derived from the AFM images are larger than the parameters based on the SAXS data. Therefore, it can be deduced that the crystals were not measured completely edge on in AFM. The difference at 97 °C is particularly large. In fact, lamellar crystals with a thickness of 129 Å (at a melt comonomer content of 5.2 mol % and a fold surface free energy of 0.05 J/m^2) would melt at 122 °C, which is far over the end melting temperature of this particular sample. This indicates that the lamellar crystals are indeed inclined in the AFM images and that—due to the presence of part of the fold surfaces—the AFM estimates of $\langle l_c \rangle$ are overestimated. Further differences between the SAXS and AFM results will be addressed in the discussion section.

The complete evolution of $\langle l_c \rangle$ based on time-resolved SAXS data is illustrated in Figure 9, together with the l_c evolution of the LPE sample, which—since for LPE the infinite lamellar model holds—equals $\langle l_c \rangle$.

The LPE sample displays a moderate surface melting[23,46] up to about 100 °C, after which l_c increases due to melting and recrystallization.[23] The copolymer $\langle l_c \rangle$ values remain constant up to 90 °C. Then they increase rapidly, probably for the same reason. However, the *D* values in Figure 8 start to increase much earlier at about 0 °C.

Below 110 and 90 °C for respectively the LPE and copolymer samples, α_S equals 1. In these temperature regions Q_{id} was divided by the product $\phi_L(1 - \phi_L)$, with ϕ_L from eq 15 for the

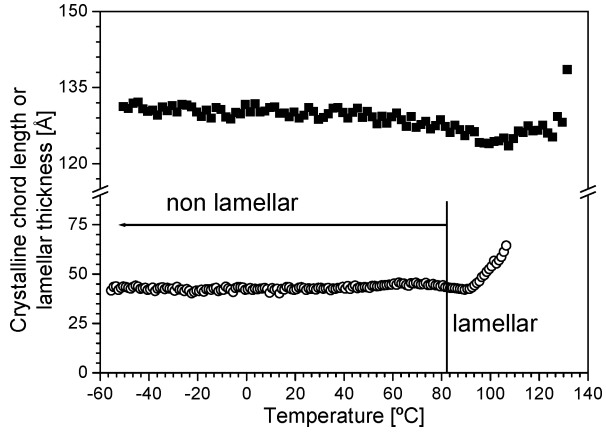

Figure 9. Temperature evolution of the average crystal chord length for the LPE (full squares) and copolymer sample (open circles).

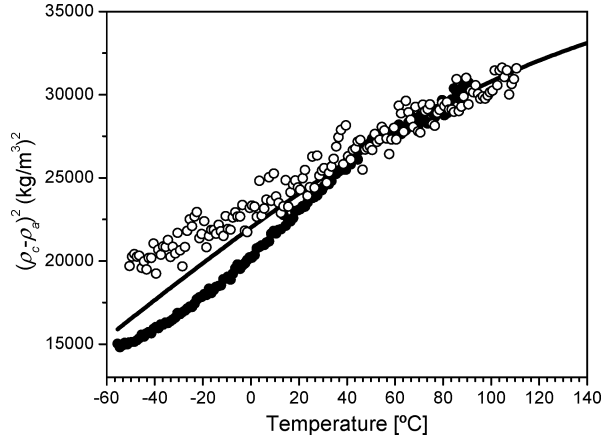

Figure 10. SAXS-based contrast factor for the LPE (open circles) and copolymer (full circles) sample. The full line represents the contrast expected for the reference crystalline and amorphous densities.

LPE and from WAXD for the copolymer. The result, which equals $C(\rho_c - \rho_a)^2$, is represented in Figure 10 and was scaled to a best agreement with the reference contrast $(\rho_c - \rho_a)^2$, based on eqs 10 and 11.

Accordingly, in this scaling procedure we obtain a best estimate for C with as a result contrast factors $(\rho_c - \rho_a)^2$. For both samples the experimental contrast factors deviate at the lowest temperatures from the reference contrast represented by a full line. The positive deviation in the case of LPE was attributed to a deviation in ρ_a. Taking the ρ_c values based on the Swan formalism, contrast-based LPE ρ_a values were obtained and are represented in Figure 11.

The arrow at about 17 °C indicates the temperature at which in calorimetry experiments deviating heat capacity values are observed for the amorphous component in semicrystalline LPE.[47] Below this temperature amorphous LPE is believed to slowly vitrify, and this is confirmed by the slower increase of ρ_a with decreasing temperature below 17 °C. Accordingly, a similar deviation in ρ_a is also expected at the copolymer glass transition temperature. Indeed, at about −50 °C[48] there is a positive upturn in the copolymer contrast function of Figure 13 with decreasing temperature. Associating this upturn with the evolution in ρ_a while otherwise keeping the reference ρ_a values, SAXS contrast based copolymer ρ_c values are obtained as illustrated in Figure 11 (open squares).

For all temperatures the LPE ρ_c values based on WAXD are nearly identical to the Swan reference values (eq 10). In contrast, the WAXD-based copolymer ρ_c values, included in Figure 11

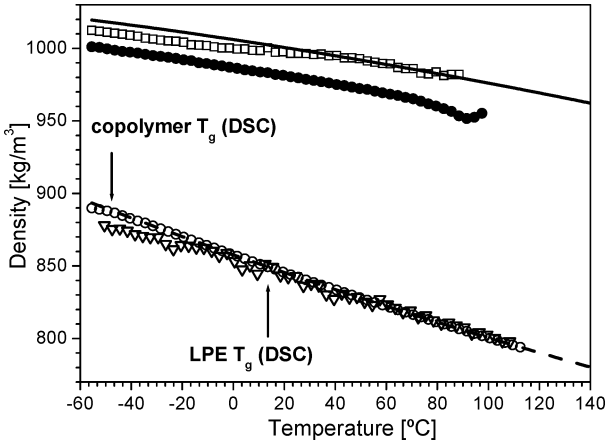

Figure 11. Crystalline reference density after Swan (full line), the WAXD-based crystalline density for the copolymer (full circles), the reference liquid like amorphous phase density (dashed line), the SAXS contrast based crystalline density for the copolymer (open squares), and the SAXS contrast based amorphous LPE (open triangles) and copolymer (open circles) densities. The arrows highlight the glass transition temperatures of the two polymers and the associated amorphous phase density deviation from the liquid reference line.

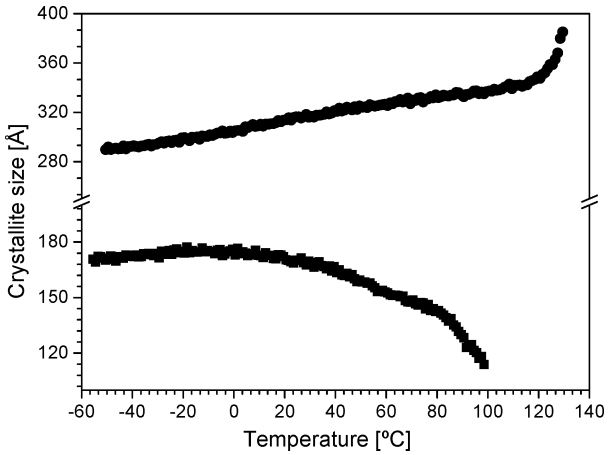

Figure 12. Apparent crystal size associated with the width of the 110 reflection during heating for the LPE (full circles) and copolymer (full squares) samples.

for comparison, are clearly different form those based on the SAXS contrast. In the conversion of the WAXD mass fraction crystallinity to a volume fraction, reference densities were used and these volume crystallinities were used to calculate densities from Q_{id}. There is an apparent inconsistency since the reference and SAXS-based crystal density values are different. However, the conversion from mass to volume fraction is not sensitive to such small density differences, in contrast to Q_{id} which depends on the square of the density difference. In other words, when the Q_{id} based densities are used in the mass to volume conversion, this iterative operation leaves the Q_{id}-based densities nearly unchanged.

WAXD 110 peak width analysis, in combination with eq 9, allows the determination of the crystal sizes (see Figure 12). The LPE crystal grain size increases whereas the copolymer grain size decreases.

Lower magnification AFM images show that, after quenching, both the LPE and copolymer sample exhibit a spherulitic arrangement of the crystals, with spherulite diameters between 5 and 10 μm (see Figure 13).

Entities of this size should scatter visible light. However, only LPE exhibits the classical spherulite like Hv (4-fold clover leave) and Vv patterns. These patterns are persistent up to the end of

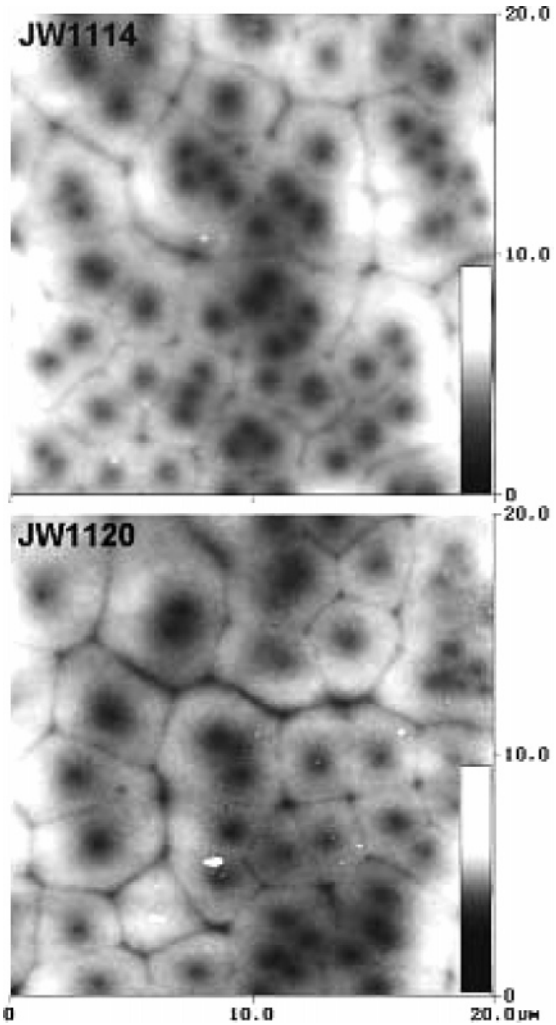

Figure 13. Tapping mode AFM topographic images of quenched LPE (JW1114) and copolymer (JW1120) at room temperature. The gray scale corresponds to the height range 0−400 nm for JW1114 and 0−700 nm for JW1120.

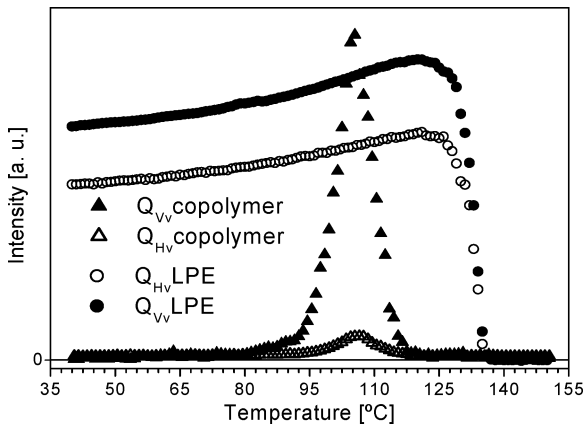

Figure 14. SALS Q_{Vv} and Q_{Hv} of quenched copolymer and LPE samples according to the included legend during heating run.

melting process. Then they simultaneously collapse. The associated integrated intensities, Q_{Hv} and Q_{Vv}, are shown in Figure 14. Note the slight increase as a function of temperature prior to the final collapse.

The copolymer Q_{Hv} and Q_{Vv} values exhibit a different behavior. At the lowest temperatures there is no scattering at all in the range of observation, neither in Hv nor in Vv. Only above 80 °C (the temperature at which, according to SAXS data, laterally extended lamellar crystals are present) scattering starts to develop and decreases again when melting becomes pronounced. We attribute the absence of light scattering intensity to the absence of orientational correlation; i.e., P_2 in eqs 1 and 2 equals zero due to the presence of highly branched crystals with random orientation.

For the LPE sample the ratio Q_{Vv}/Q_{Hv} is close to 4/3 at all temperatures, as expected for space-filling spherulites.[49] In contrast for the copolymer this ratio at high temperature is markedly larger, pointing at crystallinity heterogeneity: the first term in eq 2 contributes when $\phi_{sp} < 1$.

4. Discussion

4.1. LPE. LPE samples used in this work form classical, spherulitically arranged, orthorhombic lamellar crystal stacks when cooled at about 1000 °C/min. The crystalline density decreases due to thermal expansion and above the glass transition region the amorphous density behaves like that of liquid polyethylene. The lamellae display moderate surface melting upon heating. At the highest temperatures these lamellae melt and recrystallize into slightly thicker crystals. Apparently, only at the highest temperatures the quenching induced crystals reorganize. Surface melting is believed to be a temperature reversible process that takes place without a full crystal reorganization or melting/recrystallization. However, the increase of the crystal grain size (Figure 12) and the increase of the light scattering intensities (Figure 14) point to a continuous heating-induced stabilization process. The sudden increase of the crystal grain size above 120 °C coincides with the increase of the crystal thickening as observed in SAXS experiments. Accordingly, this can also be attributed to melting and recrystallization. The slower increase at lower temperature may well be associated with a sintering of the quenching-induced crystal grains. Hugel et al.[50] found a granular substructure in freshly crystallized s-PP lamellae that fades upon annealing. Whether or not these granules are observed depends on the AFM tapping conditions.[51] Yet they seem to be a common feature as Magonov and Godovsky observed for a wide variety of polyethylene samples.[51] We found crystalline granules in this particular LPE sample even after slow high-temperature crystallization.[28] Strobl suggested that the formation and growth of lamellar crystallites is a multistep process with the formation of "native crystals" from a mesomorphic precursor phase followed by structural relaxation.[52] The native crystals are layerlike assemblies of crystal grains. The relaxation involves the migration of entanglements and, in the case of copolymers, "noncrystallizable units" away from the bulk of the crystallite toward its surface and a sintering of the blocks into mature, continuous lamellae.

It seems that by rapid cooling the LPE sample is frozen into an intermediate relaxation state. Upon heating this relaxation process continues: the crystallite grain size in Figure 12 increases. McFaddin et al.[53] also found a slight increase of the crystal grain size upon heating/annealing. The increase of the light scattering intensity seems to be due to an increase of P_2, the orientation function that describes the alignment of the crystallites with respect to the spherulite radius. The development of the crystallinity, illustrated in Figure 6, cannot account for the increase in Q_{Hv} and Q_{Vv} because this evolution would cause a decrease rather than an increase. Progressive exclusion of lattice defects (entanglements or local departures from the all-trans configuration) improves the overall polymer chain orientation in the crystals. This results in an increase of P_2. Alternatively, if one wants to associate P_2 strictly with the crystal orientation, the improved chain orientation can also be classified by an increase of δ_{cr}^0.

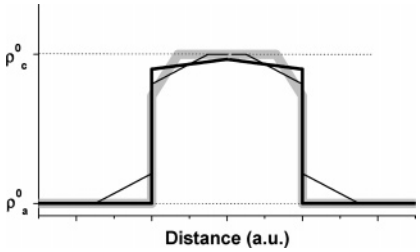

Figure 15. Three different density profiles across the crystal normal as explained in the text, with ρ_c^0 and ρ_a^0 respectively the crystalline and amorphous reference densities.

4.2. Copolymer. The observed copolymer structural features can also be discussed in terms of postponed relaxation. The amount of incorporated structural defects is larger compared to the LPE case. The presence of these defects results in deviating crystalline densities derived from WAXD or SAXS. Furthermore, the presence of crystal zones with locally different densities can account for the counter-intuitive decrease of the crystallite size in Figure 12.

Figure 15 shows the time (or temperature) development of the (electron) density profile across the crystallites. Thermal expansion is not accounted for in this time sequence.

The initial (low temperature) density profile is represented by a thick solid line and is relevant for the temperature range between −50 and 20 °C. The crystalline density is lower than the reference polyethylene density, ρ_c^0, due to the incorporation of defects, maybe even comonomer units.[54] Both SAXS and WAXD yield lower densities than ρ_c^0, but as the density is slightly declining toward the crystals borders (reflecting a slightly higher defect concentration at the crystal borders), one can expect to observe a higher density when the SAXS data are treated in terms of the corresponding ideal two-phase system. During heating the defects progressively migrate toward the surface, and above 20 °C a density profile develops like the thin full line in Figure 15. The center of the crystal is defect-free and reaches the density ρ_c^0. In contrast, the borders are defect enriched, resulting in a lower local density. Furthermore, one can also expect a densification of the amorphous regions close to the crystals due to a crowding of e.g. comonomer units.

In Figure 15 an ideal overall density profile is sketched, i.e., symmetric with respect to the crystalline amorphous interface as suggested by Strobl.[45] When SAXS profiles are analyzed in terms of the corresponding ideal two-phase structure, one obtains ρ_c^0 for the crystalline density (as is experimentally found above 20 °C in Figure 11).

Such a strict symmetry is probably not realistic, but it is unlikely that slight symmetry deviations will alter the case. According to the density profile in Figure 15, the lower density crystal fraction is larger than the dense core fraction and accordingly dominates the crystal peak positions in WAXD. This results in a WAXD crystalline density lower than ρ_c^0 and even lower than when all defects are distributed more evenly. An illustration of the progressively decreasing WAXD density evolution can be found in Figure 16.

Here the *difference* between the WAXD-based copolymer density and $\rho_c^0(T)$ is plotted. In that way one compensates for effects due to thermal expansion. We indeed find that between −50 and 60 °C the density decreases. The decrease rate becomes slightly smaller beyond the temperature (20 °C) at which a crystalline core has formed with a density equal to ρ_c^0, pointing to an equilibrated state of relaxation. Above 60 °C, this decrease accelerates again. This coincides with an increased melting rate (see the dashed line in Figure 6). Apparently, the least relaxed

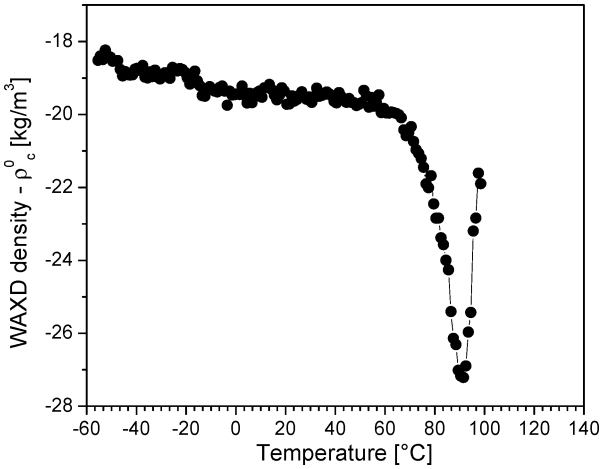

Figure 16. Evolution of the difference between the (temperature dependent) reference crystalline density, ρ_c^0, and the WAXD-based copolymer crystalline density.

crystals preferentially melt, leaving the crystals with defect-free cores to melt at higher temperatures. Between 60 and 80 °C the SAXS-based lateral crystal dimensions increase rapidly (Figure 8), pointing to preferential melting of short crystal branches or fragments, resulting in more extended lamellae. These (dominant) lamellae seem to be oriented parallel to the spherulite radii as evidenced by the development of scattered light intensity.

When the dense core has become sufficiently large, its contribution to the WAXD crystalline reflections start to dominate the WAXD peak positions. As a result, the peak position based WAXD crystalline density should increase. This is indeed observed above 90 °C (see Figure 16). The thick gray line in Figure 15 represents the corresponding profile (the amorphous densification is omitted in this case).

At 90 °C the crystal thickness also starts to increase, which we attribute to melting and recrystallization. This can be very efficient and fast because it is unlikely that melt homogenization occurs prior to recrystallization. It has been suggested earlier, based on SAXS measurements, that recrystallization after quench cooling may occur even at lower temperatures.[23] This is possible but hard to prove. In any case below 90 °C recrystallization *does not* give rise to thicker crystals. In ref 23 the ϕ_L values based on the quadratic equation were used in the SAXS analysis, assuming infinite crystal lateral dimensions. We demonstrated in the present paper that this results in a too low estimate for the crystallinity (and crystal thickness) if crystals with finite lateral dimensions are present.

Above 90 °C also more pronounced light scattering intensity is observed. This scattering is nevertheless *very* weak and much weaker than the scattering observed in the LPE sample. The intensities of the different samples are plotted in the same graph, but they should not be directly compared since they are arbitrarily scaled. (The relative difference between Q_{Hv} and Q_{Vv} for a given sample is, however, maintained.) The melting of crystal branches and fragments was selected as a cause for the appearance of scattering above 90 °C. The lack of crystal perfection also did not promote scattering at lower temperatures, in particular since the experiment on the LPE sample proves that light scattering is sensitive to crystal perfection.

The presence of crystalline zones with different densities gives rise to WAXD peak broadening on top of possible paracrystallinity or crystal size effects. Baker and Windle made a thorough analysis of polyethylene WAXD patterns and provided evidence for a partially ordered component in the broadening

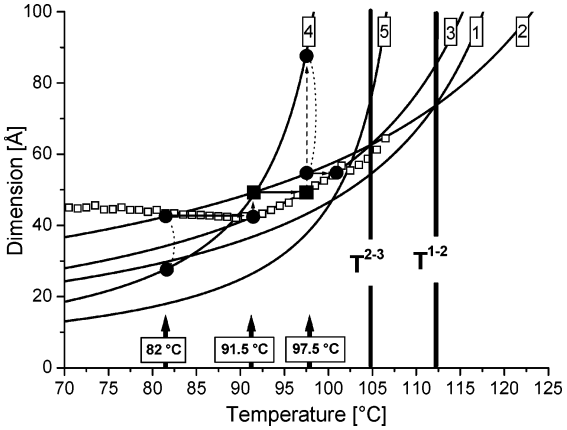

Figure 17. Stability limit (melting temperature) for fully relaxed lamellae (line 1), nonrelaxed lamellae (line 3), the thickness of the mesomorphic layers that act as crystallization precursors (line 2), the crystal grain lateral size when the orthorhombic phase is made within the mesomorphic layers via secondary nucleation involving nonrelaxed crystal surfaces (line 4), and the crystal grain lateral size when the created orthorhombic phase is fully relaxed (line 5). The open squares represent the experimental evolution of the copolymer crystal thickness (average chord length). The squares, circles, lines, and arrows are explained in the text. T^{2-3} and T^{1-2} are thresholds for particular crystallization mechanisms discussed in ref 15.

of the 110 and 200 reflections.[55] The investigated patterns contain, besides the reflections of well-ordered orthorhombic unit cells, additional low angle contributions to the 110 and 200 reflections, which are not found in the high angle peaks. These contributions were assigned to highly disordered (lack of high angle peaks) "more open" (reflections at lower angles) orthorhombic unit cells. In agreement with Figure 15 there is a range of densities associated with this open orthorhombic fraction, rather than a given specific value. In the present case we did not make any efforts to split the 110 and 200 reflections. However, the associated peak width indirectly provides information on the size spread of the crystalline unit cells. With increasing defect segregation one expects broader distributions and accordingly broader reflections. When analyzed in terms of the Scherrer equation, this (artificially) yields progressively smaller crystals, as is indeed observed and illustrated in Figure 12. For a reliable interpretation of the peak widths in terms of crystal size one needs to crystallize at a fairly high temperature where structural relaxation in terms of defect migration is fast and complete.[15,56]

According to Strobl's crystallization model[52] and more specifically the modified version,[15] orthorhombic crystals are formed via secondary nucleation within preexisting mesomorphic layers. In this conversion the mesomorphic layer thickness is preserved, and the crystal grain size is determined by the energy balance that governs secondary nucleation. The constant copolymer crystal chord length/crystal thickness in Figure 9 (prior to high-temperature recrystallization) thus reflects the thickness of the mesomorphic layers that formed during the quench (43 Å). The temperature dependence of this layer thickness was recently investigated by Cho et al.[16] and shows that layers with a thickness of 43 Å are formed at 82 °C, implying that the conversion to orthorhombic material occurs at 82 °C or below.

Figure 17 is relevant to understanding crystallization at 82 °C and melting/recrystallization *above* 82 °C for this particular copolymer with 5.2 mol % 1-octene and is reproduced from ref 15.

In this view "relaxation" points to the defect migration (side branches) away from the crystal borders into the amorphous phase. The only difference between relaxed and nonrelaxed crystal grains or lamellae is therefore associated with a difference in fold surface free energy (nonrelaxed: 0.061 J/m^2; relaxed: 0.053 J/m^2). A high defect concentration *inside* the crystals as observed at low temperature for sure would also alter the crystal enthalpy, but at 82 °C and above it is assumed (and supported by the SAXS density data in Figure 11) that all defects already have migrated toward the crystal surface and that accordingly the melting enthalpy is identical for relaxed and nonrelaxed crystals.

In the transformation of the mesomorphic layers at 82 °C (nonrelaxed) orthorhombic crystalline blocks are formed with a thickness identical to that of the mesomorphic layers (given by the full circle at 82 °C on line 2 in Figure 17) and lateral dimensions of 28 Å (the full circle on line 4 at 82 °C). These dimensions at 82 °C are connected via a dotted line in Figure 17. Grains with such small lateral dimensions correspond to a cluster of ~25 polymer stems and should give rise to extremely broad 110 and 200 WAXD reflections, in any case broader than experimentally observed (which is already increased by the unit cell density distribution as mentioned above). The data in Figure 12 thus indicate that the quenching induced grains are able to rapidly merge into larger ones. Because of block merging, the crystals transform into homogeneous lamellae that upon heating would melt at 91.5 °C. This process of crystal stabilization by block merging (reflected in an increase of the melting point) is highlighted by a horizontal arrow, connecting the full circle on line 2 with the point on line 3. Upon melting of the homogeneous orthorhombic lamellae, again mesomorphic layers are created with a thickness given by line 2 at that particular temperature (full square on line 2). Next, these mesomorphic layers transform again into orthorhombic material via secondary nuclei with lateral dimensions given by the full square at 91.5 °C on line 4, which by chance occurs at the intersection with line 2, representing the block thickness. After sintering (block merging process: see horizontal arrow) the resulting lamellae melt at 97.5 °C (full square on line 3). Upon melting at this temperature thicker mesomorphic layers are created again (full circle on line 2 at 97.5 °C) as well as larger orthorhombic grains (full circle on line 4) that merge and can melt at again a higher temperature (i.e., at the temperature of the remaining circle on line 3). When this melting, recrystallization, remelting process is fast, the crystal thickness is bound to follow line 3 as experimentally is observed (open squares in Figure 17). According to this scenario at any moment in time, nonrelaxed lamellae are created, implying that there is insufficient time or too little freedom for molecular motion for a redistribution of the comonomeric units away from the crystal surfaces into the amorphous zones during the heating run.

In contrast, during slow isothermal crystallization when crystal growth occurs in the melt, such a redistribution is possible as suggested by the presence of a separate high-temperature DSC melting peak.[15] In the present case, crystallization occurs in "molecular motion limited" semicrystalline stacks. On the other hand, grain sintering into homogeneous lamellae seems to be very fast. Certainly the fact that the lamellae and grains are formed via the melting and recrystallization of other lamellae contributes positively. One cannot expect that prior to recrystallization the melt reconfigures into an assembly of random coils. In fact, the reorganization process could very well involve a conversion from orthorhombic material to the mesomorphic phase, which after rapid layer thickening transforms again into orthorhombic material via secondary nucleation.

It is interesting to consider also the crystallization that happened during quenching *below* 82 °C. Assuming that the mesomorphic layer thickness is fixed at the value associated with its creation at 82 °C (43 Å), one can calculate (assuming 5.2 mol % 1-octene and secondary nuclei with a top surface free energy of 0.061 J/m^2)[15] that the edges of the square basis of the grains rapidly decrease from 28 Å at 82 °C to 4.3 Å at 28 °C, which is the approximate molecular cross section. Below 28 °C single chain stems easily nucleate individually. Intermediate grain sizes are involved at temperatures between 28 and 82 °C. The rapid attachment of single stems or clusters with finite lateral dimension results in disordered crystals with numerous defects included that, after or during cluster merging, will migrate out of the crystals, in particular during heating. This rapid attachment is prone to result in highly branched crystals with finite lateral dimensions, which we indeed observe. Clustered hexyl branches or chain entanglements are impurities that are avoided by the crystal growth front by which the growth changes direction (branching) or stops (finite lateral dimensions). This is a kind of cellulation, however, on a smaller length scale than usually observed in optical microscopy measurements.[57−59] Such behavior was observed by means of in-situ AFM in poly(hydroxybutyrate).[60] Alternatively, one may speculate that the mesomorphic layer scaffold was highly branched from the start. In this context the observed semicrystalline morphology thus reflects the mesomorphic layer morphology.

The motivation for carrying out the AFM experiments at 25, 80, and 97 °C is as follows: 25 °C is the lowest temperature we could reach, 80 °C occurs just before massive melting and recrystallization sets in, whereas 97 °C is in the middle of the melting−recrystallization window. Since considerably more time is spent at 97 °C in the AFM experiment compared to the scattering experiments, discrepancies can be expected in terms of crystallinity. The AFM crystallinity equals 0.42 whereas WAXD reveals only 0.12. Besides the longer time for (re)crystallization the fact that the crystals are tilted also contributes to the excess AFM crystallinity.

5. Conclusions

During rapid cooling at about 1000 °C/min LPE crystallizes into classical, spherulitically organized, semicrystalline lamellar stacks. The crystals, however, contain a number of chain conformational defects that are progressively excluded upon heating as can be deduced from the increasing light scattering intensity. Concomitantly, the crystal grain size increases and surface melting is observed. At higher temperatures some crystals melt and recrystallize. The crystalline density does not depart from perfect orthorhombic material at any temperature. The amorphous fraction is (at least partially) vitrified below ~17 °C.

In the copolymer case the devitrification above approximately −50 °C can also be derived from the amorphous density evolution based on the SAXS total scattering intensity. In addition, the highly branched crystals that were formed during quenching contain a considerable amount of defects that are fairly homogeneously distributed within the crystals. Upon heating, these defects migrate toward the crystal surface. As a result, the SAXS-based crystalline density slowly evolves to that of perfect orthorhombic material. The lower WAXD-based crystalline density values are accounted for by the presence of more open orthorhombic unit cells at the crystal borders. The heating-induced gradual diversification and spatial segregation of the crystalline unit cells over the crystal cross section also explains the increasing WAXD crystalline peak widths. During heating crystal fragments and branches preferentially melt, leading to an increase of the crystal lateral dimensions probed by SAXS.

The methodology adopted to extract the crystal lateral dimensions was also applied to the correlation functions calculated from binarized high-temperature AFM images. The reasonable agreement between the calculated and visually observed crystal lateral dimensions justifies the methodology used. Most importantly, it is shown how crystals with finite lateral dimensions produce too low crystallinity values when classical SAXS methods designed for assemblies of laterally extended lamellae are erroneously used. The disagreement between the AFM- and SAXS-based morphological parameters is mainly related to the fact that in AFM not all crystals are measured strictly edge-on. The long-term annealing involved in the AFM images is another source of disparity, in particular at the highest temperature (97 °C) were the crystals melt and recrystallize.

An increase of the WAXD crystalline density is observed, and light scattering intensity appears at high temperatures where the most stable crystals that resulted from the cooling−heating procedure melt and recrystallize. These crystals are lamellar in the classical sense as they are laterally extended, and they manage to segregate all defects to the crystal borders either during the quench cooling or during the subsequent heating run. During recrystallization into thicker lamellae at high temperature there is no time or motional freedom for a redistribution of the comonomer units away from the crystal surfaces into the amorphous phase, since only crystals are formed with a surface free energy characteristic of "nonrelaxed" crystals.

Acknowledgment. B. Goderis is a postdoctoral fellow of the Fund for Scientific Research Flanders (FWO-Vlaanderen). M. Basiura, B. Goderis, and H. Reynaers thank FWO-Vlaanderen for a research grant and support of the DUBBLE project. R. Gearba and D. A. Ivanov thank the Communauté Française de Belgique (ARC 00/05-257) for financial support.

References and Notes

(1) Eder, G.; Janeschitz-Kriegl, H. In *Material Science and Technology, Processing of Polymers*; Meijer, H. E. H., Ed.; VCH Verlagsgesellschaft GmbH: Weinheim, 1997; Chapter 5, p 313.
(2) Wagner, J.; Phillips, P. J. *Polymer* **2001**, *42*, 8999.
(3) Barham, P. J.; Jarvis, D. A.; Keller, A. *J. Polym. Sci., Polym. Phys. Ed.* **1982**, *20*, 1733.
(4) Breedon Jones, J.; Barenberg, S.; Geil, P. H. *Polymer* **1979**, *20*, 903.
(5) Hendra, P. J.; Jobic, H. P.; Holland Moritz, K. *J. Polym. Sci., Polym. Lett. Ed.* **1975**, *13*, 365.
(6) Cutler, D. J.; Glotin, M.; Hendra, P. J.; Jobic, H. P.; Holland Moritz, K.; Cudby, M. E. A.; Willis, H. A. *J. Polym. Sci., Polym. Phys. Ed.* **1979**, *17*, 907.
(7) Ding, Z.; Spruiell, J. *J. Polym. Sci., Part B: Polym. Phys.* **1996**, *34*, 2783.
(8) Magill, J. H. *Polymer* **1961**, *2*, 221.
(9) Magill, J. H. *Polymer* **1962**, *3*, 35.
(10) Supaphol, P.; Spruiell, J. *J. Polym. Sci., Part B: Polym. Phys.* **1998**, *36*, 681.
(11) Supaphol, P.; Spruiell, J. *J. Appl. Polym. Sci.* **2002**, *86*, 1009.
(12) Alamo, G. G.; Mandelkern, L. *Macromolecules* **1991**, *24*, 6480.
(13) Mathot, V. B. F.; Scherrenberg, R. L.; Pijpers, M. F. J.; Engelen, Y. M. T. In *New Trends in Polyolefin Science and Technology*; Hosoda, S., Ed.; Research Signpost: Trivandum, India, 1996; p 71.
(14) Wagner, J.; Abu-Iqyas, S.; Monar, K.; Phillips, P. J. *Polymer* **1999**, *40*, 4717.
(15) Rabiej, S.; Goderis, B.; Janicki, J. Mathot, V. B. F.; Koch, M. H. J.; Groeninckx, G.; Reynaers, H.; Gelan, J.; Wlochowicz, A. *Polymer* **2004**, *45*, 8761.
(16) Cho, T. Y.; Heck, B.; Strobl, G. *Colloid Polym. Sci.* **2004**, *282*, 825.
(17) Tashiro, K.; Imanishi, K.; Izumi, Y.; Kobayashi, M.; Kobayashi, K.; Satoh, M.; Stein, R. S. *Macromolecules* **1995**, *28*, 8477.
(18) Flory, P. J. *Trans. Faraday Soc.* **1955**, *51*, 848.

(19) Vonk, C. G.; Reynaers, H. *Polym. Commun.* **1990**, *31*, 190.
(20) Laupretre, F.; Monnerie, L.; Barthelemy, L.; Vairon, J. P.; Sauzeau, A.; Roussel, D. *Polym. Bull. (Berlin)* **1986**, *15*, 159.
(21) Pérez, E.; VanderHart, D. L.; Crist, B.; Howard, P. R. *Macromolecules* **1987**, *20*, 78.
(22) Pérez, E.; VanderHart, D. L. *J. Polym. Sci., Part B: Polym. Phys.* **1987**, *25*, 1637.
(23) Goderis, B.; Peeters, M.; Mathot, V. B. F.; Koch, M. H. J.; Bras, W.; Ryan, A. J.; Reynaers, H. *J. Polym. Sci., Part B: Polym. Phys*. **2000**, *38*, 1975.
(24) Peeters, M.; Goderis, B.; Vonk, C. G.; Reynaers, H.; Mathot, V. B. F. *J. Polym. Sci., Part B: Polym. Phys.* **1997**, *35*, 2689.
(25) Goderis, B.; Reynaers, H.; Koch, M. H. J. *Macromolecules* **2002**, *35*, 5840.
(26) Peeters, M.; Goderis, B.; Reynaers, H.; Mathot, V. B. F. *J. Polym. Sci., Part B: Polym. Phys.* **1999**, *37*, 83.
(27) Goderis, B.; Reynaers, H.; Koch, M. H. J.; Mathot, V. B. F. *J. Polym. Sci., Part B: Polym. Phys.* **1999**, *37*, 1715.
(28) Goderis, B.; Reynaers, H.; Scherrenberg, R.; Mathot, V. B. F.; Koch, M. H. J. *Macromolecules* **2001**, *34*, 1779.
(29) Stein, R. S.; Rhodes, M. B. *J. Appl. Phys.*. **1960**, *31*, 1873.
(30) Yoon, D. Y.; Stein, R. S. *J. Polym. Sci., Polym. Phys. Ed.* **1974**, *12*, 735.
(31) Ivanov, D. A.; Daniels, R.; Magonov, S. Application Note published by Digital Instruments/Veeco Metrology Group, 2001, pp 1−12. Available on line at URL: http://di.com/APPNotes_PDFs/AN45-%20HeatingStage.pdf.
(32) Ivanov, D. A.; Amalou, Z.; Magonov, S. N. *Macromolecules* **2001**, *34*, 8944.
(33) Basire, C.; Ivanov, D. A. *Phys. Rev. Lett.* **2000**, *85*, 5587.
(34) Ivanov, D. A.; Magonov, S. In *Polymer Crystallization: Observations, Concepts and Interpretations*; Sommer, J. U., Reiter, G., Eds.; Springer-Verlag: Berlin, 2003; pp 98−129.
(35) Press, W. H.; et al. *Numerical Recipes in C, The Art of Scientific Computing*; Plenum Press: New York, 1988.
(36) Ruland, W. *Colloid Polym. Sci.*. **1977**, *255*, 417.
(37) Koberstein, J. T.; Morra, B.; Stein, R. S. *J. Appl. Crystallogr.* **1980**, *13*, 34.
(38) Balta-Calleja, F. J.; Vonk, C. G. *X-ray Scattering of Synthetic Polymers*; Elsevier: Amsterdam, 1989.
(39) Bras, W.; Dolbnya, I. P.; Detollenaere, D.; van Tol, R.; Malfois, M.; Greaves, G. N.; Ryan, A. J.; Heeley, E. *J. Appl. Crystallogr.* **2003**, *36*, 791.
(40) Gabriel, A.; Dauvergne, F. *Nucl. Instrum. Methods* **1982**, *201*, 223.
(41) Dolbnya, I. P.; Alberda, H.; Hartjes, F. G.; Udo, F.; Bakker, R. E.; Konijnenburg, M.; Homan, E.; Cerjak, I.; Goedtkindt, P.; Bras, W. *Rev. Sci. Instrum.* **2002**, *73*, 3754.
(42) Alexander, L. E. *X-ray Diffraction Methods in Polymer Scince*; Robert E. Krieger Publishing Co., Inc.: Huntington, 1979; p 423.
(43) Swan, P. R. *J. Polym. Sci.* **1960**, *42*, 525.
(44) Basiura, M. Ph.D. Thesis, Catholic University of Leuven, 2005.
(45) Strobl, G.; Schneider, M. *J. Polym. Sci., Polym. Phys. Ed.* **1980**, *18*, 1343.
(46) Albrecht, T.; Strobl, G. *Macromolecules* **1995**, *28*, 5827.
(47) Mathot, V. B. F. *Polymer* **1984**, *25*, 579.
(48) Vanden Eynde, S.; Mathot, V. B. F.; Koch, M. H. J.; Reynaers, H. *Polymer* **2000**, *41*, 4889.
(49) Goderis, B.; He, Y.; Basiura, M.; de Schaetzen, G.; Mathot, V. B. F. Koch, M. H. J.; Reynaers, H. *Prog. Colloid Polym. Sci.* **2005**, *130*, 51.
(50) Hugel, T.; Strobl, G.; Thomann, R. *Acta Polym.* **1999**, *50*, 214.
(51) Magonov, S.; Godowsky, Y. *Am. Lab.* **1999**, *31*, 55.
(52) Strobl, G. *Eur. Phys. J. E* **2000**, *3*, 165.
(53) McFaddin, D. C.; Russell, K. E.; Wu, G.; Heyding, R. D. *J. Polym. Sci., Polym. Phys. Ed.* **1993**, *31*, 175.
(54) Baker, M. E.; Windle, A. H. *Polymer* **2001**, *42*, 681.
(55) Baker, A. M. E.; Windle, A. H. *Polymer* **2001**, *42*, 667.
(56) In ref 28 the isothermal crystallization of JW1120 is discussed at 97 °C. Because of an error in the angular calibration, too low densities are reported for this experiment. The peak widths and their interpretation in terms of crystal size are, however, reliable.
(57) Keith, H. D.; Padden, F. J. *J. Appl. Phys.* **1963**, *34*, 2409.
(58) el Maaty, M. I. A.; Bassett, D. C.; Olley, R. H.; Jaaskelainen, P. *Macromolecules* **1988**, *31*, 7800.
(59) el Maaty, M. I. A. *Polymer* **2002**, *43*, 6535.
(60) McMaster, T. J.; Hobbs, J. K.; Barham, P. J.; Miles, M. J. *Probe Microsc.* **1997**, *1*, 43.

MA060588F